Aalborg Universitet

Passivity-Based Stability Analysis and Damping Injection for Multiparalleled VSCs with *LCL* Filters

Xiongfei Wang, *Member, IEEE*, Frede Blaabjerg, *Fellow, IEEE*, and Poh Chiang Loh

Abstract—This paper addresses the harmonic stability resulting from the current-control interactions of the multiparalleled, *LCL*-filtered voltage-source converters. First, an alternative impedance model is proposed for the single-loop current control. The control output admittance of the converter is decomposed into a passive filter output admittance in series with an active admittance, which is dependent on the current controller and the time delay. The frequency-domain passivity theory is then applied to the active admittance for system stability analysis. It reveals that the stability region of the single-loop grid current control is not only dependent on the time delay, but affected also by the resonance frequency of the converter-side filter inductor and filter capacitor. Further on, the damping injection based on the discrete derivative controller is proposed to enhance the passivity of individual converters and thereby stabilizing the paralleled converters. Finally, simulation studies and laboratory tests validate the effectiveness of theoretical analysis and controller design.

Index Terms—Admittance, current control, damping, passivity, stability.

I. INTRODUCTION

VOLTAGE-SOURCE converters (VSCs) are widely used with renewable power generation sources [1], energy-efficient power loads [2], and flexible ac/dc transmission power systems [3]. The harmonics generated from the switching operations of VSCs may make influences on other electrical devices and may even trigger the resonance frequencies of the power system [4], [5]. Using *LCL*-filters can effectively attenuate the switching-frequency harmonics, yet the additional *LCL*-filter resonance frequency may interact with the control loops of VSCs, leading to harmonic instability phenomena [6], [7], and the subsequent resonance propagations when multiple *LCL*-filtered VSCs are connected in parallel [8], [9].

The adverse effect of the *LCL*-filter resonance on the stability of VSCs has been well documented [10]–[13]. The time delay of the digital control system, which, in the worst cases, includes one sampling period (T_s) of computational delay [14] and half sampling period $(0.5\,T_s)$ of pulse-width modulation (PWM)

delay [15], has been found to have a stabilizing effect within the single-loop grid-side current control [10], [11]. The frequency region that allows for a stable current control was then derived as a function of the time delay [11]. This finding was later extended to the single-loop converter-side current control with the opposite stable region identified [12], [13]. Given the time delay of 1.5 T_s, for example, the one-sixth of the sampling frequency $(f_s/6)$ was found as the critical frequency below the Nyquist frequency $(f_s/2)$. A stable grid-side current control can be achieved for the *LCL* resonance frequency between $f_s/6$ and $f_s/2$, whereas the converter-side current control can be designed stable for the *LCL* resonance frequency below $f_s/6$. However, this delay-dependent stability assessment assumes that the grid impedance is inductive, i.e., only single *LCL*-filter resonance is included in the current control loop, while the effect of multiple resonance frequencies in the grid impedance [16] is overlooked.

A few research works have been reported for the stability analysis of multiparalleled, *LCL*-filtered VSCs [17]–[20], [40]. The dynamic coupling of paralleled VSCs through a nonzero grid impedance challenges the stability and power quality of the system [4]–[9]. In [17], a general multiple-input multiple-output (MIMO) model was developed for the *N*-paralleled VSCs. The stability of VSCs was then decomposed as the internal stability of single VSC with an ideally zero grid impedance at the point of connection (PoC), and the external stability coming from the dynamic interactions among the paralleled VSCs and the power grid. It was further found that when the *N*-paralleled VSCs are identical, the equivalent grid impedance seen from single VSC becomes *N* times higher, and the MIMO model is simplified as the single-input single-output (SISO) transfer function. Yet, if the VSCs are different, the multivariable control theory will be required by the MIMO system, which complicates the stability analysis.

To facilitate the stability assessment at the system-level, the impedance-based approach was recently applied, which reveals a physical insight into the dynamic interactions of the paralleled VSCs [6], [8], [18]–[20]. In this method, each VSC is modeled as a Norton equivalent circuit at the PoC, which consists of a current source denoting the reference-to-output response of the current loop and the control output admittance, which models the response of the current to the PoC voltage. Thus, the internal stability of VSCs is depicted by the equivalent current source. When the VSC is internally stable, the external stability will be determined by the ratio of the control output admittance to the equivalent system admittance, including the grid admittance and the control output admittances of the other paralleled VSCs

[6], [18]. In this way, the MIMO system of the paralleled VSCs is transformed into multiple SISO transfer functions derived at the PoC of each VSC [18]. The system can be actively stabilized by shaping the control output admittances of VSCs [6].

Many active damping methods have recently been developed to stabilize the current control of *LCL*-filtered VSCs [9], [21]–[26]. Yet, only a few of them were developed to shape the VSC control output admittance [21]–[23]. Moreover, those schemes were usually designed under a given range of grid conditions. They may not work effectively with the multiparalleled VSCs and, particularly when the VSCs have different control methods or parameter variations [9], [17]. Hence, there is still lack of an admittance specification that ensures the stability of VSCs to be immune to the changes of grid conditions.

For improving the system stability robustness, the frequency-domain passivity theory [27] was introduced for grid-connected VSCs [28]–[31]. It has been shown in [28] that the VSC will not destabilize the system if its control output admittance is passive, i.e., 1) the admittance itself has no right half-plane (RHP) poles, which implies that the VSC is internally stable at the PoC and 2) the real part of the admittance is nonnegative [29]. If the grid impedance is also passive, then the whole grid-connected VSC system will be passive and stable [29]. This passivity concept is a sufficient yet not necessary stability condition, but it does allow for stable integrations of VSCs into power grids [30].

The passivity characteristic of the single-loop converter-side current control has been analyzed in [28]–[30]. The frequency region for the control output admittance having a negative real part was identified. The damping control based on feeding back the filter capacitor voltage was also developed to mitigate such a nonpassive region [30]. However, the passivity of the single-loop grid-side current control has, thus, far yet been discussed. Unlike the converter-side current control, where the filter plant is simply the converter-side inductor [28], the plant of the grid-side current control is the whole *LCL*-filter, which brings in the different passivity characteristic [31].

This paper begins with the passivity analysis of the single-loop current control for grid-connected VSCs with *LCL*-filters. Both the converter- and grid-side current control are evaluated. An alternative impedance model is proposed first, which allows the control output admittance to be decomposed into an active admittance which is affected by the current controller and time delay, and a passive output admittance of the filter plant. Thus, the nonpassive region of the control output admittance can be readily identified based on the active admittance part. The same conclusion as [28] can be drawn for the converter-side current control, where the nonpassive region is solely dependent on the time delay, which agrees with the unstable region identified by the delay-dependent stability analysis [12], [13]. However, for the grid-side current control, it has been found in this paper that the nonpassive region is not only dependent on the time delay, but affected also by the resonance frequency of the converter-side filter inductor and the filter capacitor. This consequently leads to a nonpassive region different from the converter-side current control. Moreover, unlike the delay-dependent analysis, which only considers the single *LCL*-filter resonance [11], [12],

Fig. 1. Circuit diagram of a three-phase *LCL*-filtered VSC with the single-loop current control.

the passivity analysis can also predict the stability even with a capacitive grid impedance or multiple resonance frequencies.

Then, the passivity-based damping schemes are proposed for mitigating the nonpassive region of current loops and thereby stabilizing the paralleled inverters. The damping controllers are synthesized based on the discrete derivative controller, which, instead of introducing additional control loops, are embedded into the single-loop control structure, and thus, minimizes the number of sensors. Finally, simulation studies and experimental tests demonstrate the effectiveness of the stability analysis and the damping controller design.

II. IMPEDANCE MODELING OF SINGLE-LOOP CURRENT CONTROL

A. System Description

Fig. 1 illustrates the circuit diagram of a three-phase *LCL*-filtered VSC with the single-loop current control. Either the converter-side current i_1 or grid-side current i_2 is measured for regulation [10]–[13]. A constant dc-link voltage is assumed for the sake of simplicity. The parasitic resistances of the *LCL*-filter are neglected for the worst case with zero passive damping. The phase-locked loop is used to synchronize with the PoC voltage. The synchronization bandwidth is designed to be lower than the grid fundamental frequency, in order not to induce any low-frequency oscillations [32], [33].

Since the system is assumed as balanced, the current control loops can be represented by the SISO models shown in Fig. 2. Fig. 2(a) and (b) depict the converter-side and grid-side current control diagrams, respectively, where $G_c(s)$ is the proportional + resonant current controller, and $G_d(s)$ denotes the effect of time delay, which are, respectively, expressed as

$$G_c(s) = k_p + \frac{k_i s}{s^2 + \omega_1^2} \qquad (1)$$

$$G_d(s) = e^{-1.5 T_s s} \qquad (2)$$

where the time delay of $1.5\,T_s$ is considered in this work [14], [15]. k_p and k_i are the proportional and resonant controller gains, respectively, and ω_1 is the grid fundamental frequency.

B. Proposed Impedance Model

In this subsection, an impedance model is introduced for the single-loop current control, which allows the dynamic effects of

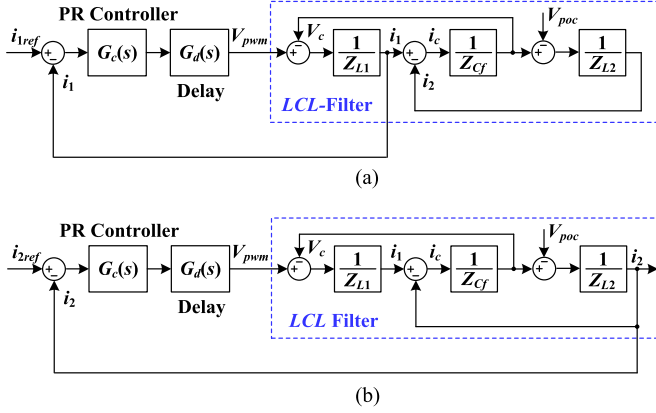Fig. 2.   Block diagram of single-loop current control. (a) Converter-side current control. (b) Grid-side current control.
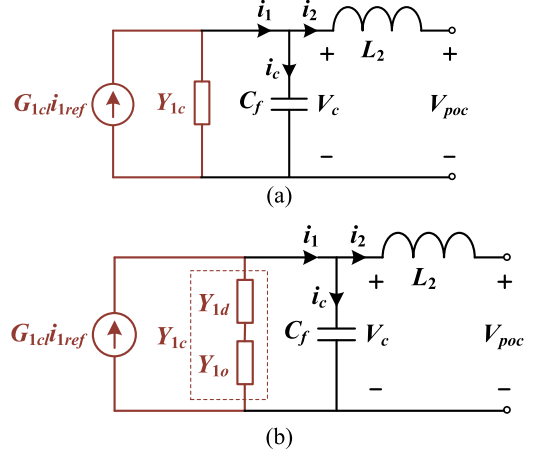

Fig. 3.   Impedance-based models for the converter-side current control. (a) Conventional impedance model. (b) Proposed impedance model.

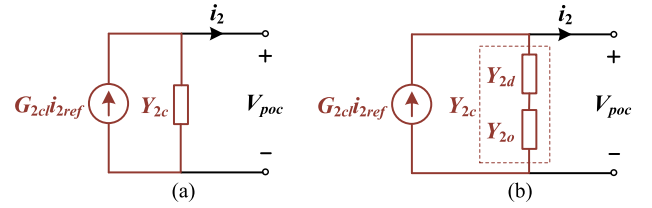Fig. 4.   Impedance-based models for the grid-side current control. (a) Conventional impedance model. (b) Proposed impedance model.

the current controller and time delay to be distinguished from the passive filter output admittance.

1) Converter-Side Current Control: To derive the impedance model for the converter-side current control, and meanwhile keep the electric property at the PoC of VSC, the control loop is closed by only including the converter-side filter inductor L_1 as the plant [34], where the voltage across the filter capacitor V_c is seen as the disturbance input. Then, the closed-loop response of the control loop can be expressed as

$$i_1 = G_{1cl}(s)i_{1\,\mathrm{ref}} - Y_{1c}(s)V_c \qquad (3)$$

where $G_{1\mathrm{cl}}(s)$ is the current reference-to-output transfer function and $Y_{1\mathrm{c}}(s)$ is the control output admittance, which are given by

$$G_{1cl}(s) = \left.\frac{i_1}{i_{1\,\mathrm{ref}}}\right|_{V_c=0} = \frac{T_1(s)}{1+T_1(s)},$$

$$T_1(s) = G_c(s)G_d(s)Y_{1p}(s) \qquad (4)$$

$$Y_{1c}(s) = \left.\frac{i_1}{V_c}\right|_{i_{1\,\mathrm{ref}}=0} = \frac{Y_{1o}(s)}{1+T_1(s)} \qquad (5)$$

$$Y_{1p}(s) = \left.\frac{i_1}{V_{\mathrm{pwm}}}\right|_{V_c=0} = \frac{1}{Z_{L1}},$$

$$Y_{1o}(s) = \left.\frac{i_1}{V_c}\right|_{V_{\mathrm{pwm}}=0} = \frac{1}{Z_{L1}} \qquad (6)$$

where $T_1(s)$ is the open-loop gain of the current loop, $Y_{1o}(s)$ is the output admittance of the inductor L_1, and $Y_{1p}(s)$ denotes the filter plant, derived from the converter output voltage V_{pwm} to i_1. Z_{L1} is the impedance of the filter inductor L_1.

By further dividing the numerator into the denominator of (5), an alternative form of the control output admittance $Y_{1\mathrm{c}}(s)$ can be obtained, which is given by

$$Y_{1c}(s) = \frac{Y_{1o}(s)}{1+T_1(s)} = \frac{1}{\frac{1}{Y_{1o}(s)}+\frac{1}{Y_{1d}(s)}},$$

$$Y_{1d}(s) = \frac{1}{G_c(s)G_d(s)}. \qquad (7)$$

It shows that the control output admittance can be decomposed as a series connection of $Y_{1o}(s)$, which itself is passive, and an active admittance, $Y_{1d}(s)$, determined by the current controller and time delay. Consequently, the effects of the digital current controller and the passive filter on the control output admittance can be separately characterized.

Fig. 3 illustrates the impedance models for the converter-side current control. Including the filter capacitor C_f and the grid-side filter inductor L_2, the overall closed-loop current response seen from the PoC can then be derived as

$$i_1 = \frac{1}{1+Y_{1c}(s)/Y_{L2C}(s)}G_{1cl}(s)i_{1\mathrm{ref}}$$
$$\qquad - \frac{Y_{1c}(s)/Y_{L2C}(s)}{1+Y_{1c}(s)/Y_{L2C}(s)}\frac{V_{\mathrm{poc}}}{Z_{L2}} \qquad (8)$$

where $Y_{L2C}(s)$ is the admittance of the paralleled filter capacitor C_f and grid-side filter inductor L_2, i.e., $Y_{L2C} = (Z_{L2}+Z_{Cf})/(Z_{L2}Z_{Cf})$, Z_{Cf}, and Z_{L2} are the impedances of C_f and L_2, respectively. Hence, the admittance ratio, $Y_{1c}(s)/Y_{L2C}(s)$, and the closed-loop gain, $G_{1cl}(s)$, determine the dynamic response of converter-side current control with an *LCL*-filter.

2) Grid-Side Current Control: Fig. 4 depicts the impedance models for the grid-side current control. Unlike the converter-side current control, the models are directly derived at the PoC of VSC and are expressed as [6]

$$i_2 = G_{2cl}(s)i_{2\,\mathrm{ref}} - Y_{2c}(s)V_{\mathrm{poc}} \qquad (9)$$

where $G_{2cl}(s)$ is the current reference-to-output transfer function and $Y_{2c}(s)$ is the control output admittance, which are derived as

$$G_{2cl}(s) = \left.\frac{i_2}{i_{2\,\mathrm{ref}}}\right|_{V_{\mathrm{poc}}=0} = \frac{T_2(s)}{1+T_2(s)},$$

$$T_2(s) = G_c(s)G_d(s)Y_{2p}(s) \tag{10}$$

$$Y_{2c}(s) = \left.\frac{i_2}{V_{\mathrm{poc}}}\right|_{i_{2\,\mathrm{ref}}=0} = \frac{Y_{2o}(s)}{1+T_2(s)} \tag{11}$$

$$Y_{2p}(s) = \left.\frac{i_2}{V_{\mathrm{pwm}}}\right|_{V_{\mathrm{poc}}=0} = \frac{Z_{Cf}}{Z_{Cf}Z_{L1}+Z_{L2}Z_{L1}+Z_{Cf}Z_{L2}} \tag{12}$$

$$Y_{2o}(s) = \left.\frac{i_2}{V_{\mathrm{poc}}}\right|_{V_{\mathrm{pwm}}=0} = \frac{Z_{Cf}+Z_{L1}}{Z_{Cf}Z_{L1}+Z_{L2}Z_{L1}+Z_{Cf}Z_{L2}} \tag{13}$$

where $T_2(s)$ is the open-loop gain of the grid-side current loop, $Y_{2o}(s)$ is the output admittance of the *LCL*-filter, and $Y_{2p}(s)$ is the filter plant, derived from the converter output voltage V_{pwm} to i_2.

Similarly, by dividing the numerator into the denominator of (11), the control output admittance can also be transformed as

$$Y_{2c}(s) = \frac{Y_{2o}(s)}{1+T_2(s)} = \frac{1}{\frac{1}{Y_{2o}(s)}+\frac{1}{Y_{2d}(s)}},$$

$$Y_{2d}(s) = \frac{Z_{Cf}+Z_{L1}}{G_c(s)G_d(s)Z_{Cf}} \tag{14}$$

which is equivalent to the output admittance of the *LCL*-filter, $Y_{2o}(s)$, in series with an active admittance, $Y_{2d}(s)$. Yet, differing from the active admittance $Y_{1d}(s)$, which is solely dependent on the current controller and the time delay, $Y_{2d}(s)$ is also affected by the converter-side filter inductor L_1 and filter capacitor C_f.

III. PASSIVITY-BASED STABILITY ANALYSIS

A. Passivity of Single-Loop Current Control

The passivity concept, which was first introduced in electric network theories [27], has been widely used to characterize the terminal behaviors of dynamic systems, which store or dissipate energy [35]. It provides a sufficient, yet not necessary, stability condition for interconnected dynamic systems. A system will be stable and passive if each subsystem is passive seen from its terminal [27], [36], [37].

For the single-loop current control of VSCs, its frequency-domain passivity is described based on the impedance models shown in Figs. 3 and 4 [28]–[31]. The current control is passive if:
  1) the control loop is internally stable seen from the PoC, i.e., $G_{1cl}(s)$ or $G_{2cl}(s)$ has no RHP poles;
  2) the control output admittance, $Y_{1c}(j\omega)$ or $Y_{2c}(j\omega)$, has a nonnegative real part, i.e., Re$\{Y_{1c}(j\omega)\} \geq 0$, $\forall\omega$, or Re$\{Y_{2c}(j\omega)\} \geq 0$, $\forall\omega$, which implies that the phase of $Y_{1c}(j\omega)$ or $Y_{2c}(j\omega)$ is within $[-90°, 90°]$.

Since the output admittance of the filter plant, $Y_{1o}(j\omega)$ or $Y_{2o}(j\omega)$, is passive, the passivity of current control will depend on the real part of the active admittance, i.e., Re$\{Y_{1d}(j\omega)\}$ or Re$\{Y_{2d}(j\omega)\}$, provided that the current loop is internally stable seen from the PoC.

The R gain of the current controller $G_c(s)$, k_i, is designed for zero steady-state error at the fundamental frequency, it, thus, has little phase contribution at the higher crossover frequency of the current loop [25], [38]. The expressions of the active admittance $Y_{1d}(j\omega)$ and $Y_{2d}(j\omega)$ can then be simplified by neglecting the R gain of $G_c(s)$, which are given by

$$Y_{1d}(j\omega) = \frac{1}{k_p}e^{j1.5\omega T_s} = \frac{1}{k_p}\left[\cos(1.5\,T_s\omega)+j\sin(1.5\,T_s\omega)\right] \tag{15}$$

$$Y_{2d}(j\omega) = \frac{1-L_1C_f\omega^2}{k_p}e^{j1.5T_s\omega}$$

$$= \frac{1-L_1C_f\omega^2}{k_p}\left[\cos(1.5\,T_s\omega)+j\sin(1.5\,T_s\omega)\right] \tag{16}$$

where the delay function $G_d(s)$ is transformed into the triangular form by using Euler's formula.

From (15), it is noted that the negative real part of $Y_{1d}(j\omega)$ is a function of time delay, which appears in the frequency region $(f_s/6, f_s/2)$ and can be narrowed by reducing the delay involved in the control loop. If the delay is ideally zero, the converter-side current loop will be passive below the Nyquist frequency. This agrees with the passivity-based analysis in [28]–[30].

In contrast, for the grid-side current control, (16) elaborates that the negative real part of $Y_{2d}(j\omega)$ is not only determined by the time delay, but also affected by the resonance frequency of L_1 and C_f, i.e., f_{L1C} [31]. A negative real part is introduced into $Y_{2d}(j\omega)$ between f_{L1C} and $f_s/6$. Yet, if f_{L1C} is designed exactly at $f_s/6$, the real part of $Y_{2d}(j\omega)$ will be nonnegative below the Nyquist frequency, and the passivity of the grid-side current control will be ensured [37].

B. Stability of Single VSC With Converter-Side Current Control

For illustrating the implication of the passivity property, the internal stability of the converter-side current control for single VSC is analyzed first, and then the external stability of the grid-side current control for the paralleled VSCs is evaluated. Table I gives the main circuit parameters of the system.

Fig. 5(a) shows the frequency response of the open-loop gain $T_1(s)$, where the R gain of $G_c(s)$ is neglected and the P gain, k_p, is designed for a 45° of phase margin (PM). $G_{1cl}(s)$ is, thus, stable, and the internal stability at the PoC will then be dependent on the admittance ratio, $Y_{1c}(s)/Y_{L2C}(s)$.

Fig. 5(b) plots the frequency responses for the admittances $Y_{1c}(s)$ and $Y_{L2C}(s)$, respectively. It can be seen that the phase of $Y_{1c}(s)$ is below $-90°$ from $f_s/6$ to $f_s/2$, which implies a negative real part and an inductive imaginary part in the frequency range. This agrees with the nonpassive region predicted by (15).

TABLE I
MAIN CIRCUIT PARAMETERS

Symbol	Electrical Constant	Value
V_g	Grid voltage	400 V
f_1	Grid fundamental frequency	50 Hz
L_g	Grid inductance	2 mH
f_{sw}	Converter switching frequency	10 kHz
f_s	Converter sampling frequency	10 kHz
V_{dc}	Converter dc-link voltage	730 V
L_1	LCL-filter—converter-side inductor	2.7 mH
L_2	LCL-filter—grid-side inductor	0.9 mH
C_f	LCL-filter—capacitor	9.4 μF
f_{L1C}	$L_1 C_f$-filter resonance frequency	0.999 kHz
f_r	LCL-filter resonance frequency	1.998 kHz
L_c	Cable inductance	0.48 mH/km
C_c	Cable capacitance	0.46 μF/km
r_c	Cable resistance	0.025 Ω/km

In contrast, the phase of $Y_{L2C}(s)$ in the nonpassive region exhibits a capacitive behavior, which, together with $Y_{1c}(s)$, forms an LC circuit with a negative resistance. As a consequence, the parallel LC resonance will be triggered and amplified by the negative real part of $Y_{1c}(s)$, when the magnitude responses of $Y_{1c}(s)$ and $Y_{L2C}(s)$ intersect in the nonpassive region.

It is worth noting that the admittances $Y_{1c}(s)$ and $Y_{L2C}(s)$ basically constitute a minor feedback loop [39]. The admittance ratio, $Y_{1c}(s)/Y_{L2C}(s)$, is the open-loop gain of this minor feedback loop, and the phase difference at the intersection point of the magnitude responses of $Y_{1c}(s)$ and $Y_{L2C}(s)$ indicates the PM of the minor feedback loop. A negative PM will be yielded when the phase difference at the intersection point is over 180° [40]. Hence, the instability occurs when $Y_{L2C}(s)$ is capacitive in the nonpassive region of $Y_{1c}(s)$. On the other hand, if $Y_{L2C}(s)$ is inductive in the nonpassive region, no LC resonant circuit will be formed, and the system will be kept stable with a positive PM. This further explains why the passivity is a necessary, yet not sufficient, stability condition.

C. Stability of Multiparalleled VSCs With Grid-Side Current Control

Fig. 6 illustrates the per-phase diagram of four paralleled, LCL-filtered VSCs, which are interconnected via power cables to the grid. The 1 km Π-equivalent model is used to represent the cable, and the parameters are also given in Table I.

Substituting the impedance models for the paralleled VSCs, the impedance-based equivalent circuit can be drawn in Fig. 7. The equivalent system admittance for single VSC is represented by $Y_{1load}(s)$ or $Y_{2load}(s)$, which includes the cable impedance, the grid impedance, and the control output admittances of the other paralleled VSCs.

The effect of the equivalent system admittance on the closed-loop response can then be derived as follows:

$$i_1 = \frac{1}{1 + Y_{1c}(s)/Y_{1load}(s)} G_{1cl}(s) i_{1ref}$$

$$i_2 = \frac{1}{1 + Y_{2c}(s)/Y_{2load}(s)} G_{2cl}(s) i_{2ref} \qquad (17)$$
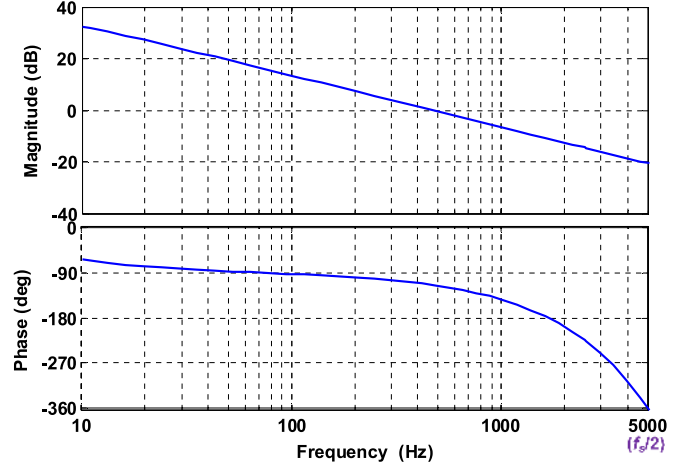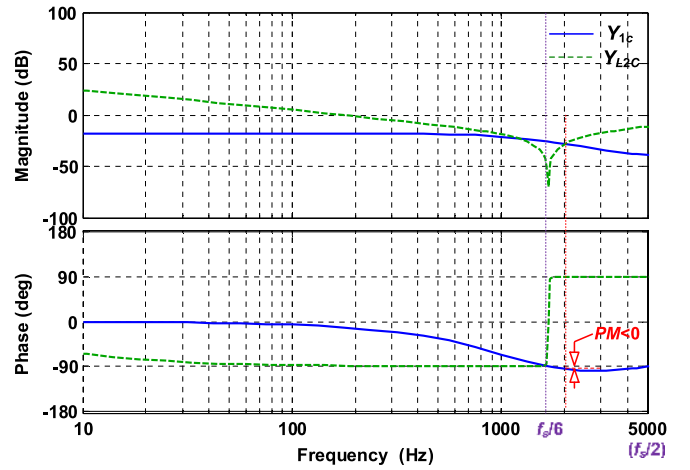
Fig. 5. Frequency responses of converter-side current control. (a) Open-loop gain $T_1(s)$. (b) Control output admittance $Y_{1c}(s)$ and the admittance $Y_{L2C}(s)$.

where the control output admittances and the equivalent system admittances constitute a minor feedback loop. The admittance ratio, $Y_{1c}(s)/Y_{1load}(s)$ or $Y_{2c}(s)/Y_{2load}(s)$, is the open-loop gain of the minor feedback loop, and it determines the external stability of the paralleled VSCs, provided that $G_{1cl}(s)$ and $G_{2cl}(s)$ are internally stable. Since the LCL-filter resonance frequency is above $f_s/6$, the converter-side current control is unstable, which has been analyzed in Fig. 5. Only the external stability of the paralleled VSCs with the grid-side current control is evaluated below.

Fig. 8 plots the frequency responses of the open-loop gain $T_2(s)$ and the control output admittance $Y_{2c}(s)$ for the grid-side current control. An internally stable current response at the PoC can be observed in Fig. 8(a) [10], [11]. Fig. 8(b) shows that the phase of $Y_{2c}(s)$ is out of [−90°, 90°] from f_{L1C} to $f_s/6$, which verifies the derived nonpassive region in (16). Moreover, unlike $Y_{2c}(s)$ shown in Fig. 5(b), the phase of $Y_{2c}(s)$ exhibits a capacitive behavior in the nonpassive region, which may destabilize the system with an inductive grid impedance. On the other hand, if the phase of $Y_{2c}(s)$ is below −90° in the nonpassive region, the current loop will be unstable with a capacitive grid
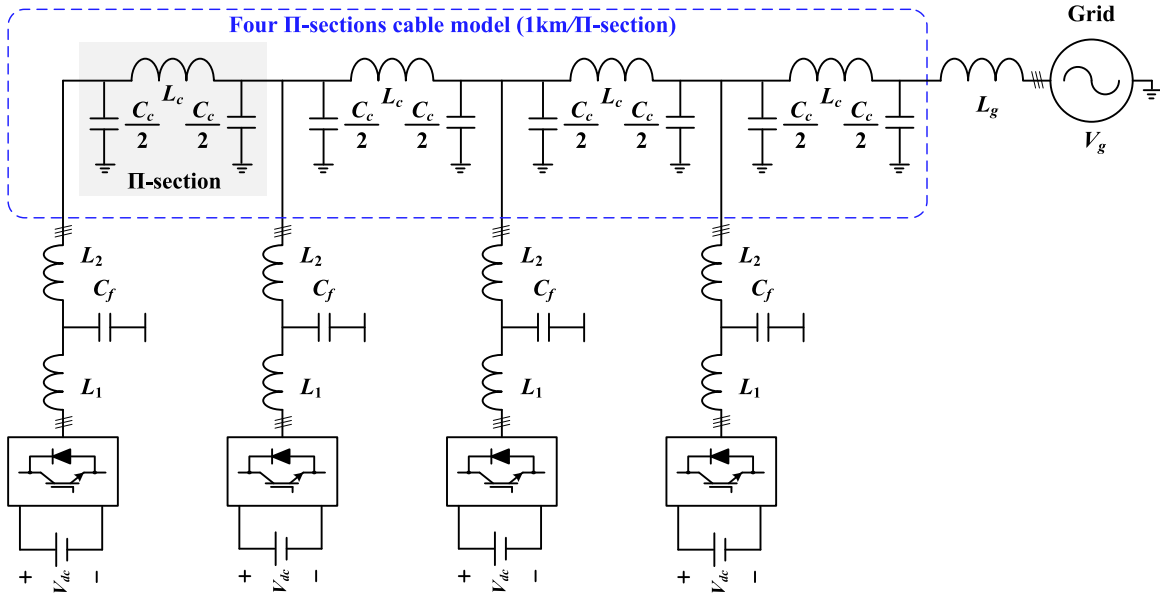
Fig. 6.   Per-phase diagram of four paralleled, three-phase *LCL*-filtered VSCs, which are interconnected with power cables to the power grid.
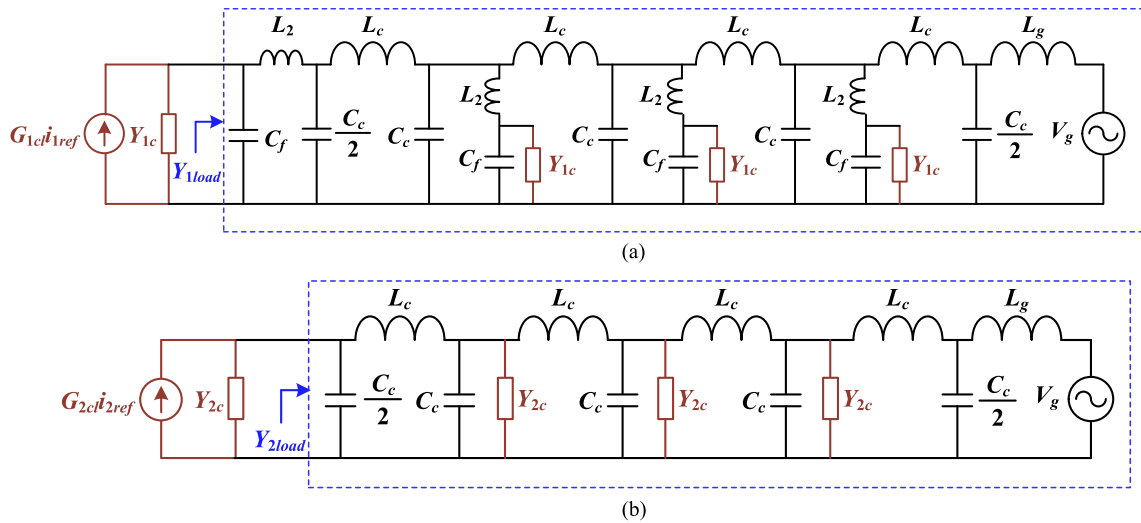

Fig. 7.   Impedance-based models of four paralleled VSCs. (a) Converter-side current control. (b) Grid-side current control.

impedance [31]. Hence, compared with the delay-dependent analysis which only considers the inductive grid impedance [10], [11], the passivity-based analysis also predicts the stable region under a capacitive grid condition. This region is not only dependent on the time delay, but affected also by the *LCL*-filter design.

Fig. 9 compares the frequency responses of $Y_{2c}(s)$ and the equivalent system admittance $Y_{2\text{load}}(s)$ given in Fig. 7(b). It is seen that multiple resonance frequencies are introduced in the load admittance $Y_{2\text{load}}(s)$, due to the control output admittances of the other paralleled VSCs and cables. Multiple intersections of their magnitude responses fall into the nonpassive region of grid-side current control, and three intersection points have the phase difference out of 180°, which imply the negative PM of the minor feedback loop [40]. Hence, instead of the single *LCL*-filter resonance shown in Fig. 5, the current control interactions of the paralleled VSCs and cables tend to cause resonances at multiple frequencies.

IV. PASSIVITY-BASED DAMPING INJECTION

For addressing the instability issues with the multiparalleled VSCs, a passivity-based damping control strategy is proposed in this section. Unlike the passivity-based damping controller reported in [30], the approach is based on the discrete derivative controller, which is embedded within the single-loop current control structure. This section presents first the damping control structures and their underlying principles, and then elaborates the design guidelines by means of the discrete *z*-domain root locus and the continuous frequency-domain passivity analysis.

(a)

(b)
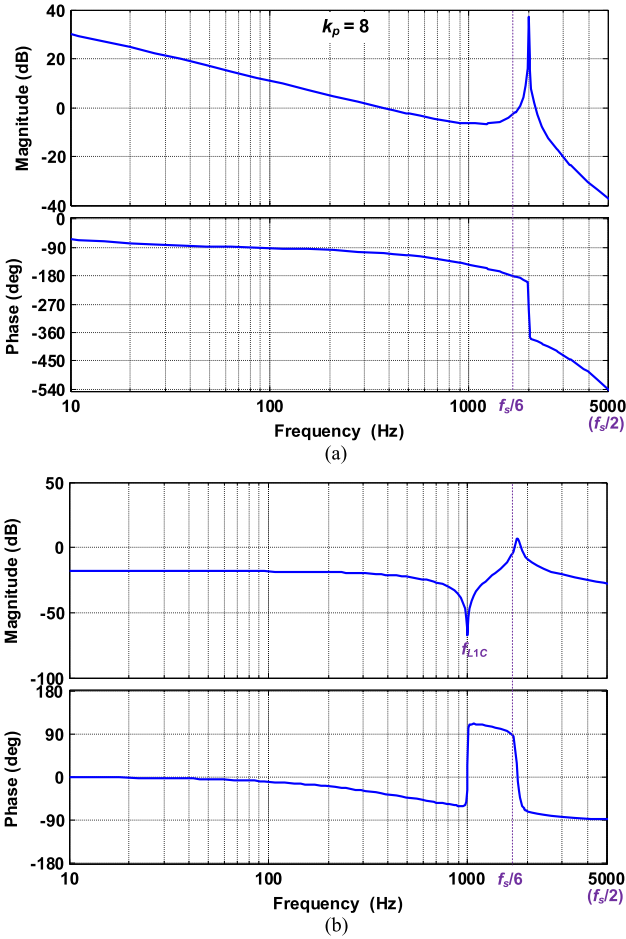
Fig. 8. Frequency responses of grid-side current control loop. (a) Open-loop gain $T_2(s)$. (b) Control output admittance $Y_{2c}(s)$.
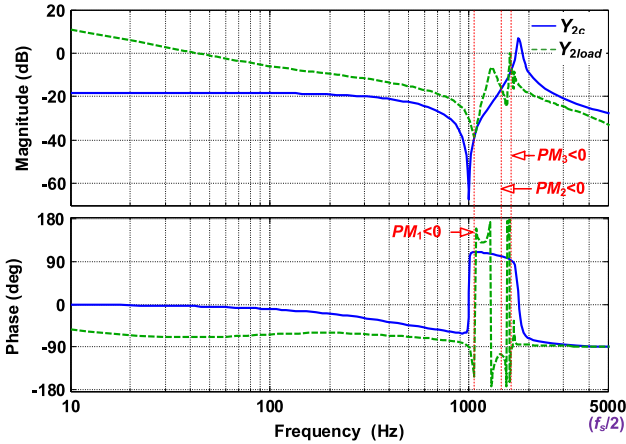
Fig. 9. Frequency responses of the control output admittance $Y_{2c}(s)$ and the equivalent load admittance $Y_{2\text{load}}(s)$.

A. Control Principles

Fig. 10 illustrates the block diagrams of the damping control methods in the discrete z-domain. Instead of using additional control loops, the damping controllers are embedded within the single-loop control structure.
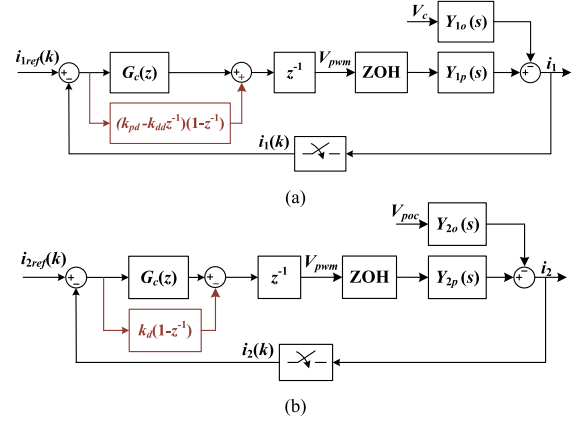
Fig. 10. Block diagrams of the proposed damping control methods. (a) Converter-side current control. (b) Grid-side current control.

Fig. 10(a) depicts the damping controller with the converter-side current control, where the general idea is to mitigate the delay effect by using an Euler derivative controller in series with an additional zero compensation. The passivity enhancement by the damping controller is illustrated by replacing k_p in (15) with k_p + damping controller, and then substituting $e^{-T_s s}$ for z^{-1}. This leads to

$$\text{Re}\left\{ \frac{1}{Y_{1d}(j\omega)} \right\} = (k_p + k_{pd})\cos(1.5\,T_s\omega)$$

$$- (k_{pd} + k_{dd})\cos(2.5\,T_s\omega)$$

$$+ k_{dd}\cos(3.5\,T_s\omega) \qquad (18)$$

where the real part of $1/Y_{1d}$ is used for predicting the passivity of current control for computational simplicity since the sign of $\text{Re}\{1/Y_{1d}(j\omega)\}$ is equal to that of $\text{Re}\{Y_{1d}(j\omega)\}$. Compared with (15), it is clear that with the injection of the damping controller, the passivity of the converter-side current control is not only dependent on the time delay, but determined also by the values of k_p and the damping controller coefficients, i.e., k_{pd} and k_{dd}. The nonpassive region can, thus, be narrowed by appropriately tuning these three parameters.

The damping controller with the grid-side current control is shown in Fig. 10(b). Unlike the converter-side current control, a negated Euler derivative controller is used to shift the delay-dependent frequency, $f_s/6$ toward the resonance frequency of L_1 and C_f, f_{L1C}, and thus, the nonpassive region shown in Fig. 8(b) can be narrowed. To elaborate, k_p in (16) is substituted by the k_p + the damping controller, and z^{-1} is replaced by $e^{-T_s s}$. Also, for the sake of simplicity, the sign of $\text{Re}\{1/Y_{2d}(j\omega)\}$ is used for the analysis, which is given by

$$\text{Re}\left\{ \frac{1}{Y_{2d}(j\omega)} \right\} = \frac{f(k_d/k_p)}{1 - L_1 C_f \omega^2}$$

$$f(k_d/k_p) = (1 - k_d/k_p)\cos(1.5\,T_s\omega) + \cos(2.5\,T_s\omega)k_d/k_p. \qquad (19)$$

It is noted that both k_p and the damping controller gain, k_d, affect the passivity of the grid-side current control, besides the time delay and f_{L1C}. This fact consequently adds an additional
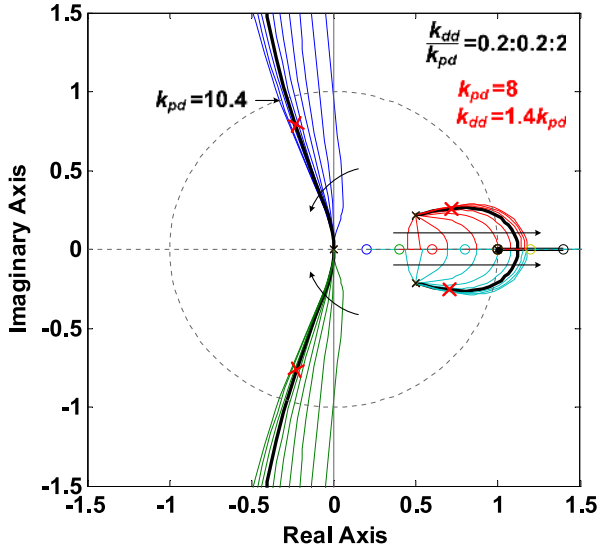
Fig. 11. Closed-loop pole trajectories of the converter-side current control with the damping controller.

degree of freedom for shaping the passivity of the control loop, compared with (16).

B. Passivity-Based Parameter Tuning

According to the passivity conditions, the current control with the damping controllers should first be designed internally stable (with the zero grid impedance), and then the damping controller parameters can be tuned for mitigating the nonpassive region.

From Fig. 10, the open-loop gains of the current control loops with the damping controllers can be derived as following:

$$T_{1d}(z) = \left[k_p + (k_{pd} - k_{dd}z^{-1})(1 - z^{-1})\right]z^{-1}z_{ZOH}\{Y_{1p}(s)\} \tag{20}$$

$$T_{2d}(z) = \left[k_p - k_d(1 - z^{-1})\right]z^{-1}z_{ZOH}\{Y_{2p}(s)\} \tag{21}$$

where $T_{1d}(z)$ and $T_{2d}(z)$ are the open-loop gains for converter-side and grid-side current control, respectively. k_{dd} and k_{pd} are the damping controller coefficients in the converter-side current control. k_d is the negated Euler derivative damping controller gain with the grid-side current control. The R gain k_i in $G_c(z)$ is neglected. The PWM delay is included by applying the zero-order hold (ZOH) transformation to the filter plants of control loops. Hence, based on (18)–(21), the passivity-based design of damping controllers can be divided into two steps:

1) First, the z-domain root locus analysis is performed based on the damped open-loop gains derived in (20) and (21), in order to identify the stability boundary for the current control to be internally stable.
2) Then, according to the frequency-domain passivity analysis in (18) and (19), the controller parameters are further tuned to mitigate the nonpassive region of the current control.

1) Converter-Side Current Control: To further illustrate the controller design procedure, Fig. 11 plots the root loci, based on (20), for the converter-side current control, where the proportional gain k_p of the current controller $G_c(z)$ is chosen as the

same value as in Fig. 5. The closed-loop poles are moved along with the increase of k_{pd} in the damping controller. The closed-loop pole trajectory is shifted by sweeping the ratio k_{dd}/k_{pd} from 0.2 to 2 at a step of 0.2, where the direction is indicated by the arrow. It is clear that the closed-loop poles are initially within the unit circle with $k_{pd} = 0$, which agrees with Fig. 5. As k_{pd} increases, the poles can still be kept in the unit circle, which implies that the system can be designed internally stable with the damping controller. Yet, the stability limit of k_{pd} is reduced with the increase of the ratio k_{dd}/k_{pd}, and the maximum k_{pd} for $k_{dd}/k_{pd} = 2$ is identified as $k_{pd} = 10.4$.

Based on the stability boundary identified in Fig. 11, the controller parameters are further tuned to improve the passivity of the converter-side current control. Fig. 12 plots the three-dimensional figures based on (18), where the ratio k_{dd}/k_{pd} varies with three values to see the change of the frequency region with a negative $\text{Re}\{1/Y_{1d}(j\omega)\}$. With the lower values of k_p/k_{pd} in Fig. 12(a) and (b), two nonpassive regions are introduced with the increase of k_{dd}/k_{pd}. In contrast, for the higher value of k_p/k_{pd}, the nonpassive region is constrained to high frequencies, but the upper frequency limit of the passive region is reduced, which is below $0.3 f_s$ in Fig. 12(c). Moreover, given a value of k_p/k_{pd}, the increase of k_{dd}/k_{pd} can widen the passive region, yet it does also reduce the limit of k_{pd} for the internal stability, as identified in Fig. 11. Hence, a compromise is made in tuning the controller parameters, i.e., $k_p = 8$, $k_p/k_{pd} = 1$, and $k_{dd}/k_{pd} = 1.4$, to which the corresponding closed-loop poles are marked in Fig. 11.

It is worth noting that the passivity enhancement for the converter-side current control is not affected by the passive filter parameters. This is because the nonpassive region is only dependent on the time delay of the control loop and controller parameters. This fact has been explained in (15) and (18). Yet, the variation of the inductor L_1 will affect the internal stability, similar to the current control of *L*-filtered VSCs [38], where a significant reduction of the filter inductance may cause unstable responses with a negative gain margin.

2) Grid-Side Current Control: Fig. 13 shows the closed-loop pole trajectories of the grid-side current control with both the P gain k_p of current controller $G_c(z)$ and the damping controller gain k_d included. The closed-loop poles are forced to move with the increase of k_p, and the pole trajectories are plotted when the ratio k_d/k_p is swept from 0 to 2.1 at a step of 0.3.

Beginning with $k_d/k_p = 0$, it can be seen that the closed-loop poles are kept within the unit circle, which implies that the grid-side current loop can be designed internally stable without the active damping. This is matched with the continuous frequency-domain analysis in Fig. 8. However, as the increase of k_d/k_p, the movement of the root loci indicates that a stable current control can still be obtained with the negated damping controller.

Then, the controller parameters can be further tuned based on (19) to mitigate the nonpassive region of the grid-side current control. Since the nonpassive region is also affected by the resonance frequency f_{L1C}, k_d/k_p needs to be tuned for a positive $f(k_d/k_p)$ at the frequencies below f_{L1C} and a negative
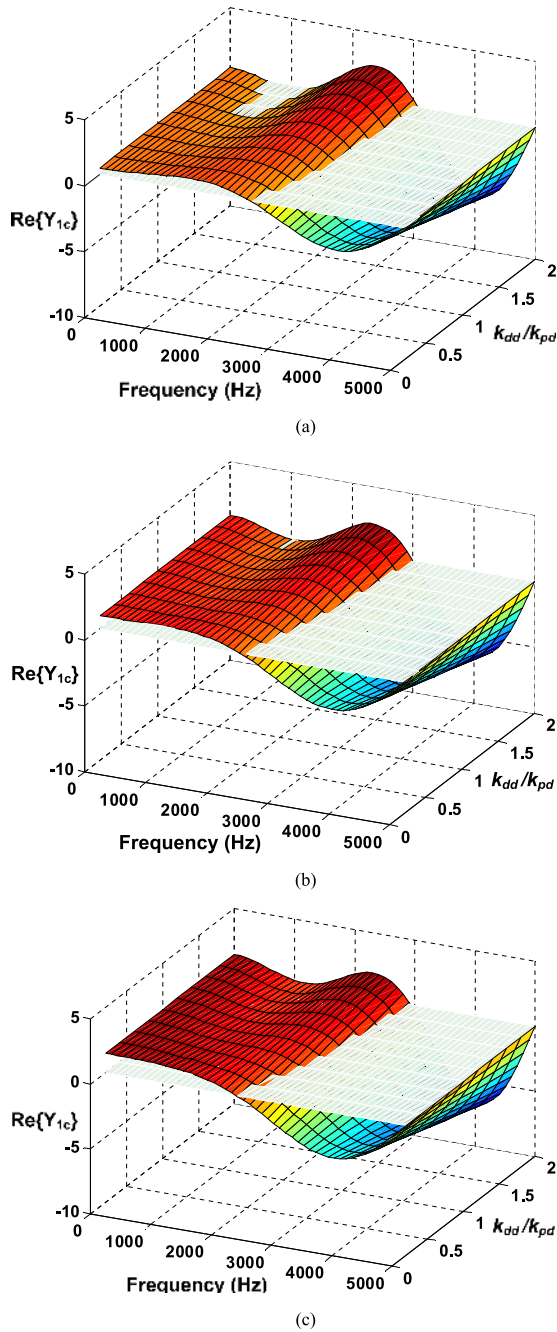
Fig. 12. Passivity analysis for the converter-side current control with the damping controller. (a) $k_p/k_{pd} = 0.5$. (b) $k_p/k_{pd} = 1$. (c) $k_p/k_{pd} = 1.5$.
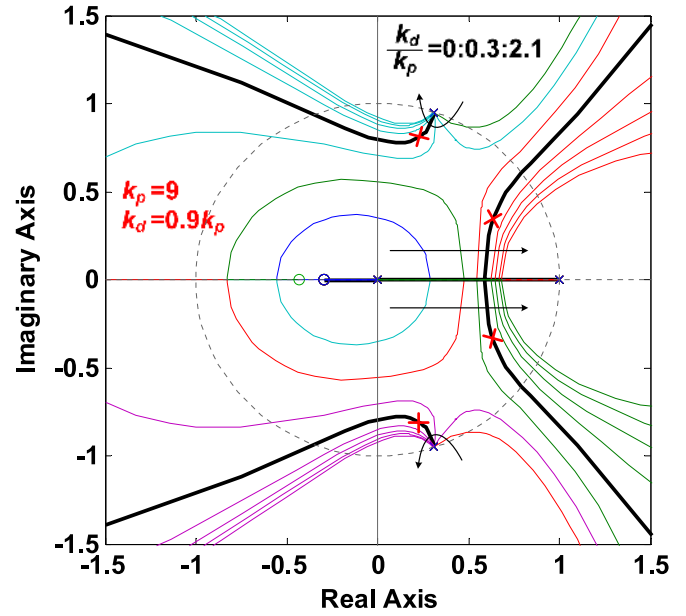

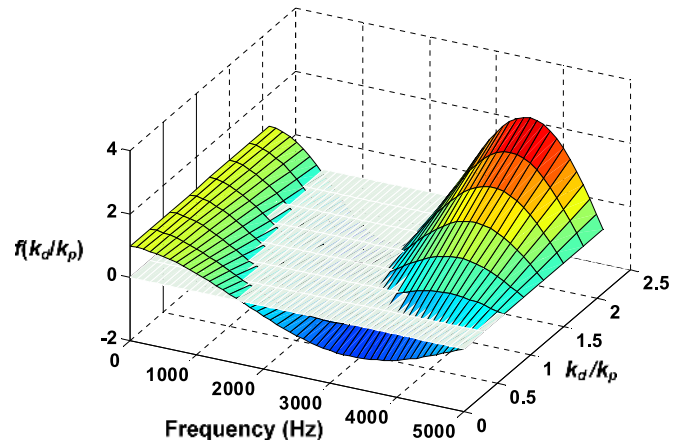Fig. 13. Closed-loop pole trajectories of the grid-side current control with the damping controller.

Fig. 14. Passivity analysis of grid-side current control with the damping controller, i.e., the effect of k_d/k_p on the sign of $f(k_d/k_p)$.

$f(k_d/k_p)$ at the frequencies above f_{L1C}. Fig. 14 illustrates how the frequency region with a negative $f(k_d/k_p)$ is changed with the varying ratio k_d/k_p. As the increase of k_d/k_p, the frequency region with the negative $f(k_d/k_p)$ is shifted toward the origin. Hence, if the lower frequency limit for $f(k_d/k_p) \leq 0$ is chosen above f_{L1C}, the nonpassive region nearby the resonance frequency f_{L1C} will be mitigated, yet it will appear at the frequencies above the upper frequency limit for $f(k_d/k_p) \leq 0$. In this paper, the value of k_d/k_p is chosen as 0.9 for a compromise. The value of k_p is selected as 9, based on Fig. 13, for a proper damping of the current loop.

Unlike the converter-side current control, the passivity-based parameter tuning is dependent on the filter inductor L_1 and filter capacitor C_f for the grid-side current control. Consequently, the filter parameter variation will affect the passivity of the grid-side current control. Fig. 15 illustrates the effect of the variation of filter inductor L_1 ($\pm$ 0.2 p.u.) on the controller performance. Fig. 15(a) plots the effects of different L_1 on the internal stability of the grid-side current control. The movements of closed-loop poles caused by the different L_1 indicate that the system can be kept internally stable. Fig. 15(b) then compares the frequency responses of $Y_{2c}(s)$ with the different L_1. It is seen that a small nonpassive region is added around the resonance frequency f_{L1C}, due to the dependence of the passivity on the resonance frequency f_{L1C}.
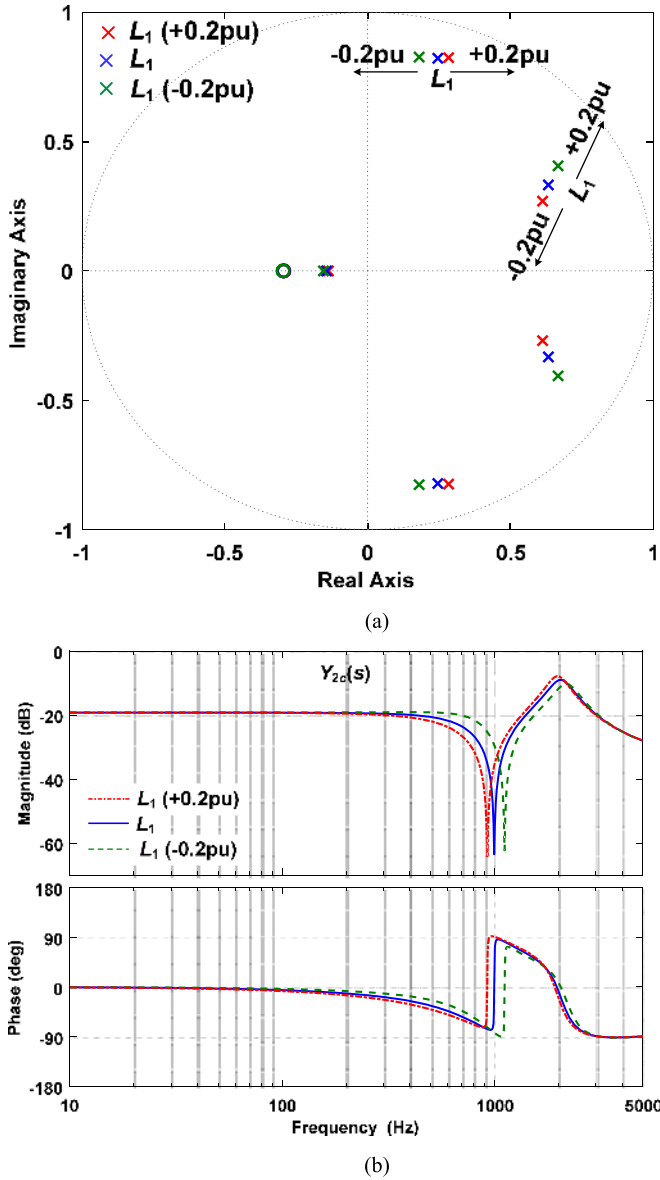
(a)

(b)

Fig. 15. Effect of the filter inductor L_1 variation (± 0.2 p.u.) on the controller performance of the grid-side current control. (a) Pole-zero map of grid-side current control with zero grid impedance. (b) Frequency responses of $Y_{2c}(s)$.

C. Stabilizing Effects of Damping Controllers

The stabilizing effects of damping controllers are analyzed based on the impedance models of paralleled VSCs in Fig. 7. Fig. 16(a) and (b) plot the frequency responses of the control output admittance and the equivalent system admittance for the converter- and grid-side current control loops, respectively. The effects of damping controllers are included in the admittances. It is obvious that the phase difference at the intersection points of their magnitude responses is below 180° in both cases. This implies that the system is kept stable in both cases. Moreover, Fig. 16(a) illustrates that $Y_{1c}(s)$ has a phase response out of $[-90°, 90°]$ at the frequencies closed to $0.3 f_s$, which agrees with Fig. 12(b). Also the frequency response of $Y_{2c}(s)$ shown in Fig. 16(b) demonstrates an enlarged passive region compared with Fig. 8.

(a)

(b)
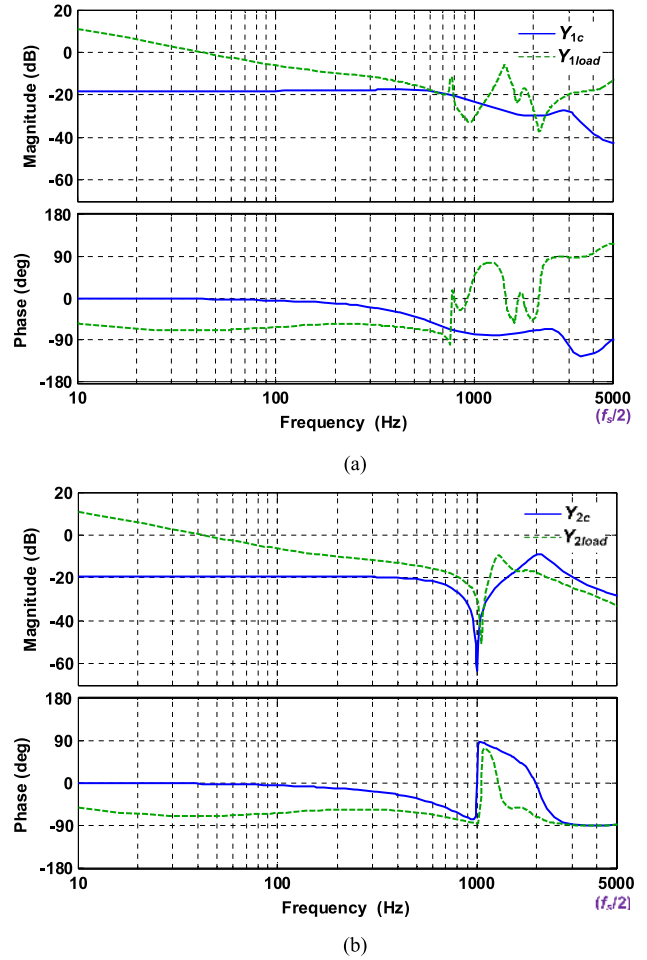
Fig. 16. Frequency responses of the control output admittances, $Y_{1c}(s)$ and $Y_{2c}(s)$, and the equivalent system admittances, $Y_{1\text{load}}(s)$ and $Y_{2\text{load}}(s)$, after using the damping controllers. (a) Converter-side current control. (b) Grid-side current control.

TABLE II
CONTROLLER PARAMETERS

Symbol	Converter-Side Current Control	Value
k_p	Proportional gain of current controller	8
k_i	Resonant gain of current controller	600
k_{pd}	Damping controller gain	8
k_{dd}	Damping controller gain	11.2
Symbol	Grid-Side Current Control	Value
k_p	Proportional gain of current controller	9
k_i	Resonant gain of current controller	600
k_d	Damping controller gain	8.1

V. SIMULATIONS AND EXPERIMENTAL RESULTS

A. Simulation Studies

For validating the theoretical analysis and the performances of the damping controllers, time-domain simulations, based on the four paralleled VSCs shown in Fig. 7, are performed using Simulink and PLECS Blockset. The circuit parameters given in
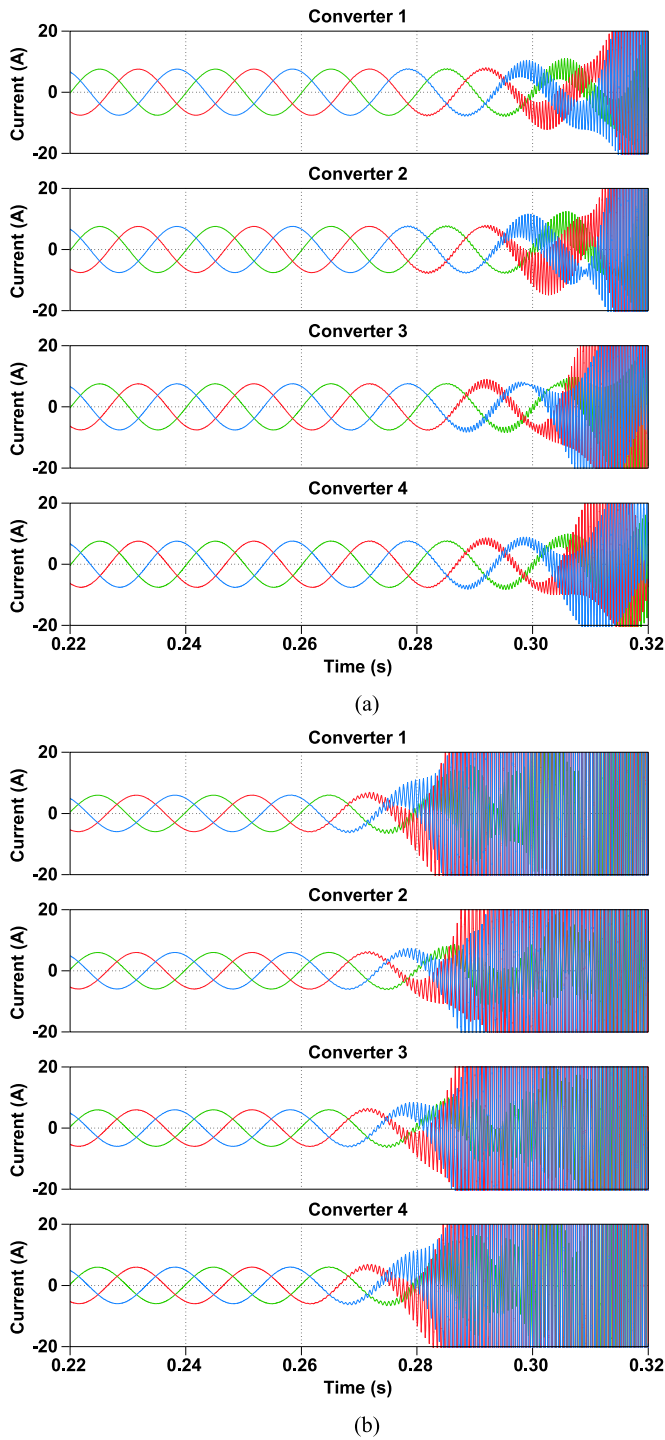
Fig. 17. Simulated grid-side currents of four paralleled VSCs with and without the damping controllers. (a) Converter-side current control. (b) Grid-side current control.
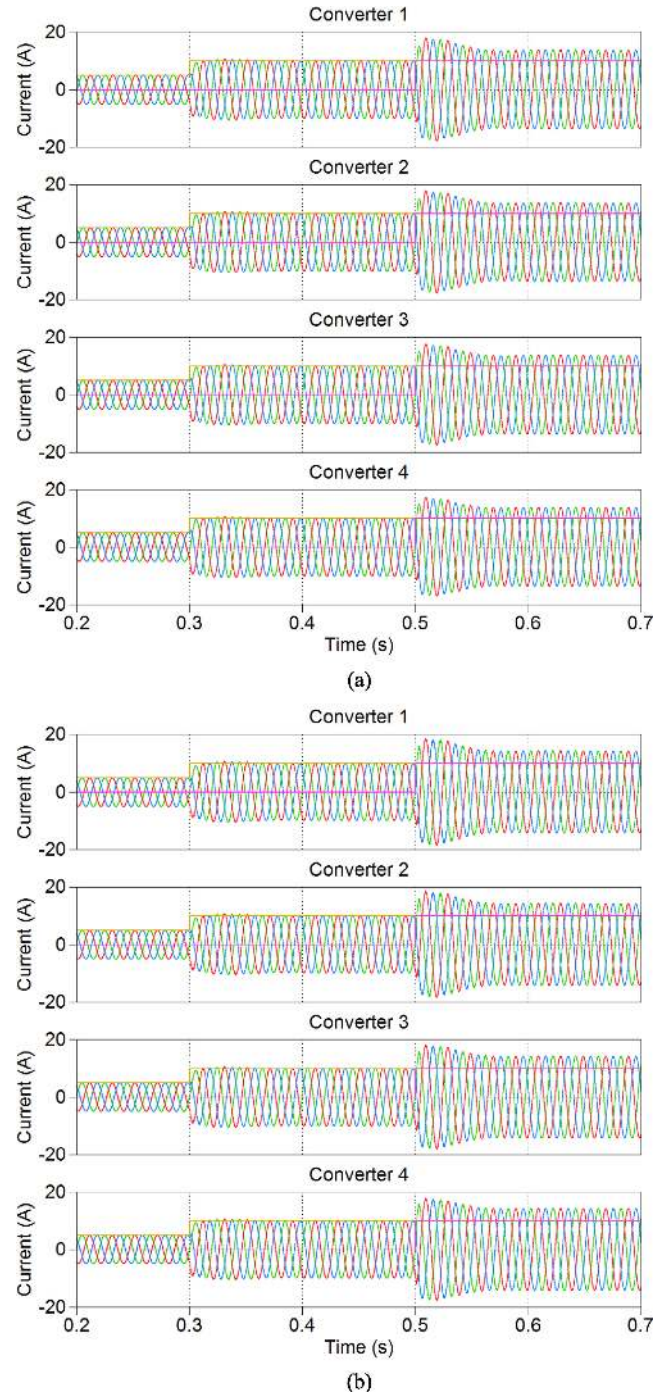

Fig. 18. Simulated step responses of grid-side currents of four paralleled VSCs with the damping controller included. (a) Converter-side current control. (b) Grid-side current control.

Table I are used. Table II summarizes the controller parameters designed in the previous sections.

Fig. 17(a) and (b) depict the simulated grid currents of four paralleled VSCs with the converter-side and grid-side current control, respectively. The damping controllers are deactivated at the time instant of 0.26 s. The system gets destabilized in both cases, which agree with the stability analysis in Figs. 5 and 9.

Fig. 18(a) and (b) depict the simulated step responses for the converter-side and grid-side current control with the damping controller enabled. Two step responses are evaluated, which are 1) the step response of the d-axis current reference, i_{dref}, from 5 to 10 A at the time instant of 0.3 s and 2) the step response of the q-axis current reference, i_{qref}, from 0 to 10 A at the time instant of 0.5 s. A good transient response can be observed with the converter-side and grid-side current control.

Fig. 19. Hardware picture of the experimental setup with three paralleled inverters.
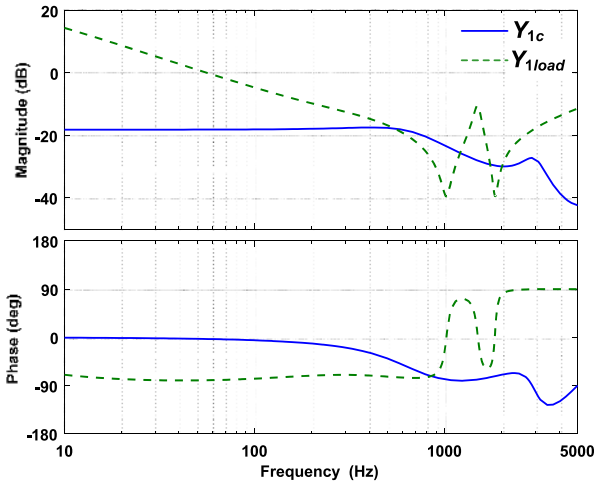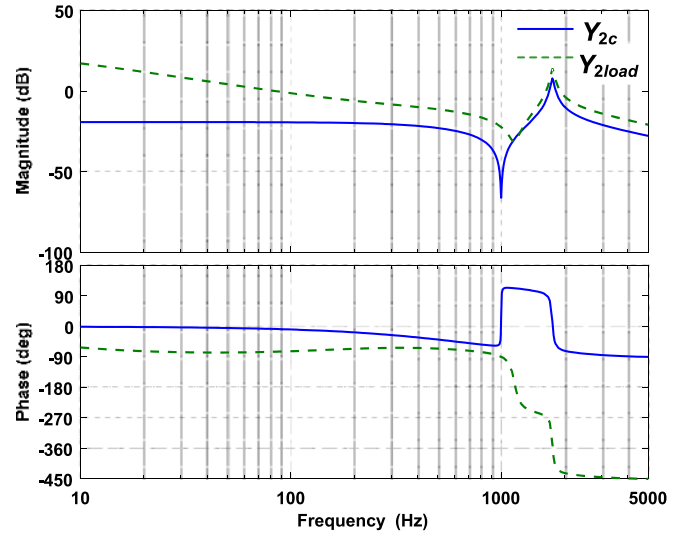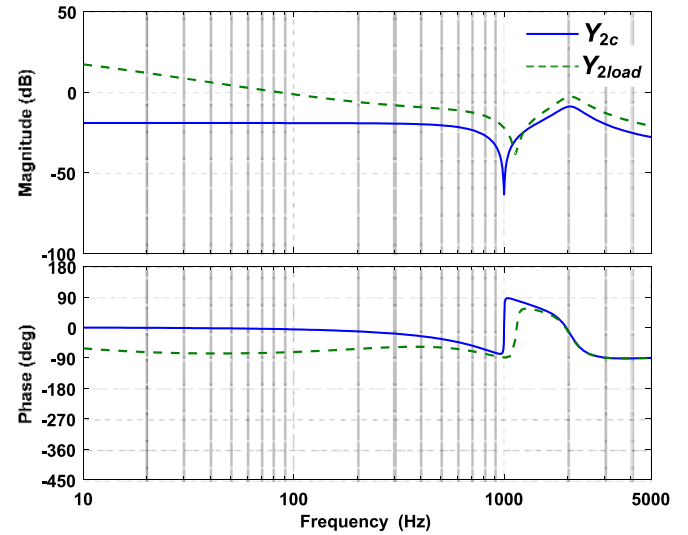

Fig. 20. Frequency responses of the control output admittances $Y_{1c}(s)$ and the equivalent system admittances, $Y_{1\text{load}}(s)$, for the converter-side current control used in the experimental system.

B. Experimental Results

Experimental tests with three paralleled, *LCL*-filtered VSCs are carried out. The VSCs are directly (cable-less) connected to the point of common coupling (PCC). The hardware picture of the laboratory test setup is shown in Fig. 19, where the same circuit and controller parameters as the simulations are adopted. Three Danfoss frequency converters, which are powered by the constant dc voltage sources, are controlled as VSCs. The control systems are implemented in a dSPACE DS1007 system, where

(a)

(b)

Fig. 21. Frequency responses of the control output admittances $Y_{2c}(s)$ and the equivalent system admittances $Y_{2\text{load}}(s)$ for the grid-side current control used in the experimental system. (a) Without the damping controller. (b) With the damping controller.

the high-speed 16 bit A/D board, DS2004, is used for sampling the voltage and currents, and the digital waveform output board, DS5101, is used for the PWM generation.

Fig. 20 shows the frequency responses of the control output admittance $Y_{1c}(s)$ and the equivalent system admittance $Y_{1\text{load}}(s)$ for the converter-side current control under tests. The damping controller is included. Differing from Fig. 16(a), there are no cable impedances included in $Y_{1\text{load}}(s)$. It is seen that the system is stabilized by using the passivity-based damping controller in each VSC.

Fig. 21 shows the frequency responses of the control output admittance $Y_{2c}(s)$ and the equivalent system admittance $Y_{2\text{load}}(s)$ for the grid-side current control in the experiment. An unstable interaction of the paralleled VSCs can be observed
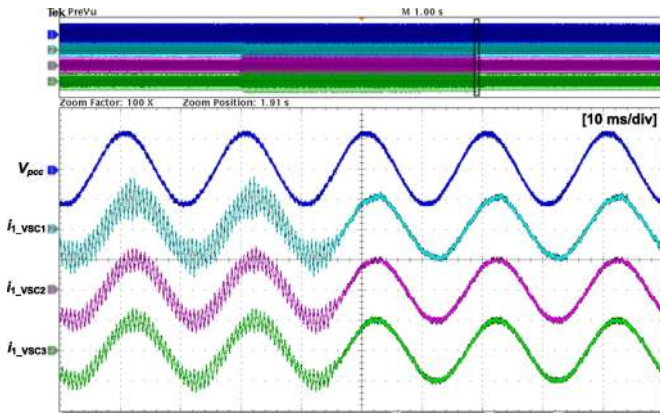
Fig. 22. Measured PCC (line-to-line) voltage, and the phase-A grid currents of three paralleled VSCs with the converter-side current control. i_2: [5 A/div]. V_{pcc}: [500 V/div].
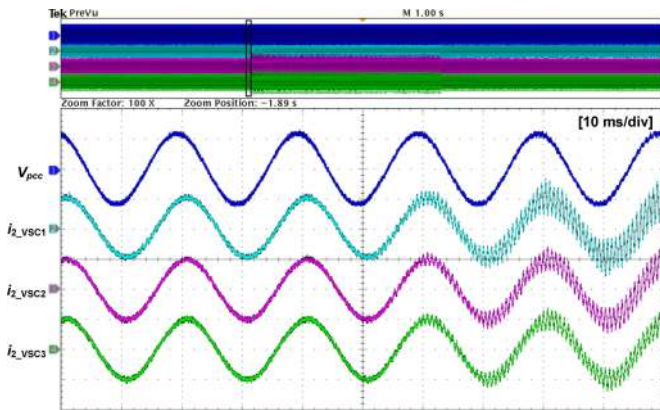

Fig. 23. Measured PCC (line-to-line) voltage, and the phase-A grid currents of three paralleled VSCs with the grid-side current control. i_2: [5 A/div]. V_{poc}: [500 V/div].

in Fig. 21(a), whereas Fig. 21(b) shows that the damping controller can stabilize the system.

The measured PCC voltage (line-to-line) and the per-phase grid current waveforms for the converter-side current control are given in Fig. 22. The zoom-in view of the waveforms at the instant of enabling the damping controller closely matches with the frequency-domain analysis in Fig. 20. Since the line-to-line voltage is measured at 500 V/div, a little oscillation can be seen in the PCC voltage. Fig. 23 shows the measured waveforms for the grid-side current control, where a zoom-in view of the test results at the instant of deactivating the damping controller is provided. The unstable response confirms again the theoretical analysis and the controller design.

VI. CONCLUSION

This paper has discussed the passivity of single-loop current controls for grid-connected VSCs with *LCL*-filters. It has been shown that the control output admittance of the converter can be decomposed as the passive open-loop *LCL*-filter admittance in series with an active admittance term affected by the current controller and time delay. Such a decomposition facilitates the

controller design for improving the passivity of the individual VSCs and consequently stabilizing the system. Further on, the active admittance of the grid-side current control revealed that its passivity is affected by both the time delay and the *LCL*-filter parameters. This is different from the passivity of the converter-side current control. The stability implication of the passivity analysis has also been elaborated. It has been shown that the instability arises when an *LC*-resonance circuit with a negative resistance is formed by the control output admittance and the equivalent system admittance of the VSC. The passivity-based damping control schemes have further been developed and the results have validated their st+abilizing performances.

REFERENCES

[1] F. Blaabjerg, Z. Chen, and S. B. Kjaer, "Power electronics as efficient interface in dispersed power generation systems," *IEEE Trans. Power Electron.*, vol. 19, no. 5, pp. 1184–1194, Sep. 2004.

[2] T. M. Jahns and V. Blasko, "Recent advances in power electronics technology for industrial and traction machine drives," *Proc. IEEE*, vol. 89, no. 6, pp. 963–975, Jun. 2001.

[3] N. Flourentzou, V. G. Agelidis, and G. D. Demetriades, "VSC-based HVDC power transmission systems: An overview," *IEEE Trans. Power Electron.*, vol. 24, no. 3, pp. 592–602, Mar. 2009.

[4] J. H. Enslin and P. J. Heskes, "Harmonic interaction between a large number of distributed power inverters and the distribution network," *IEEE Trans. Power Electron.*, vol. 19, no. 6, pp. 1586–1593, Nov. 2004.

[5] E. Mollerstedt and B. Bernhardsson, "Out of control because of harmonics—An analysis of the harmonic response of an inverter locomotive," *IEEE Control Syst.*, vol. 20, no. 4, pp. 70–81, Aug. 2000.

[6] X. Wang, F. Blaabjerg, and W. Wu, "Modeling and analysis of harmonic stability in an AC power-electronics-based power system," *IEEE Trans. Power Electron.*, vol. 29, no. 12, pp. 6421–6432, Dec. 2014.

[7] M. Liserre, R. Teodorescu, and F. Blaabjerg, "Stability of photovoltaic and wind turbine grid-connected inverters for a large set of grid impedance values," *IEEE Trans. Power Electron.*, vol. 21, no. 1, pp. 263–272, Jan. 2006.

[8] F. Wang, J. Duarte, M. Hendrix, and P. Ribeiro, "Modelling and analysis of grid harmonic distortion impact of aggregated DG inverters," *IEEE Trans. Power Electron.*, vol. 26, no. 3, pp. 786–797, Mar. 2011.

[9] P. Brogan, "The stability of multiple, high power, active front end voltage sourced converters when connected to wind farm collector system," in *Proc. Euro. Conf. Power Electron. Appl.*, 2010, pp. 1–6.

[10] J. Yin, S. Duan, and B. Liu, "Stability analysis of grid-connected inverter with LCL Filter adopting a digital single-loop controller with inherent damping characteristic," *IEEE Trans. Ind. Informat.*, vol. 9, no. 2, pp. 1104–1112, May 2013.

[11] S. G. Parker, B. P. McGrath, and D. G. Holmes, "Regions of active damping control for LCL Filters," *IEEE Trans. Ind. Appl.*, vol. 50, pp. 424–432, Jan./Feb. 2014.

[12] C. Zou, B. Liu, S. Duan, and R. Li, "Influence of delay on system stability and delay optimization of grid-connected inverters with LCL filter," *IEEE Trans. Ind. Informat.*, vol. 10, no. 3, pp. 1775–1784, Aug. 2014.

[13] J. Wang, J. Yan, L. Jiang, and J. Zou, "Delay-dependent stability of single-loop controlled grid-connected inverters with LCL filters," *IEEE Trans. Power Electron.*, vol. 31, no. 1, pp. 743–757, Jan. 2016.

[14] S. Buso and P. Mattavelli, *Digital Control in Power Electronics*, San Francisco, CA, USA: Morgan & Claypool Publisher, 2006.

[15] D. M. Van de Sype, K. D. Gusseme, F. D. Belie, A. P. Van den Bossche, and J. A. Melkebeek, "Small-signal z-domain analysis of digitally controlled converters," *IEEE Trans. Power Electron.* vol. 21, no. 2, pp. 470–478, Mar. 2006.

[16] F. Fuchs and A. Mertens, "Prediction and avoidance of grid-connected converter's instability caused by wind part typical, load-varying grid resonance," in *Proc. IEEE Energy Convers. Congr. Expo.*, 2014, pp. 2633–2640.

[17] J. Agorreta, M. Borrega, J. Lopez, and L. Marroyo, "Modeling and control of N-paralleled grid-connected inverters with LCL filter coupled due to grid impedance in PV plants," *IEEE Trans. Power Electron.*, vol. 26, no. 3, pp. 770–785, Mar. 2011.

[18] X. Wang, F. Blaabjerg, M. Liserre, Z. Chen, J. He, and Y. Li, "An active damper for stabilizing power-electronics-based AC systems," *IEEE Trans. Power Electron.*, vol. 29, no. 7, pp. 3318–3329, Jul. 2014.

[19] X. Wang, F. Blaabjerg, Z. Chen, and W. Wu, "Resonance analysis in parallel voltage-controlled distributed generation inverters," in *Proc. 28th Annu. IEEE Appl. Power Electron. Conf. Expo.*, 2013, pp. 2977–2983.

[20] X. Wang, F. Blaabjerg, and P. C. Loh, "An impedance-based stability analysis method for paralleled voltage source converters," in *Proc. IEEEInt. Power Electron. Conf. (IPEC-Hiroshima 2014 - ECCE ASIA)*, 2014, pp. 1529–1535.

[21] J. Dannehl, M. Liserre, and F. Fuchs, "Filter-based active damping of voltage source converters with LCL filter," *IEEE Trans. Ind. Electron.*, vol. 58, no. 8, pp. 3623–3633, Aug. 2011.

[22] M. Cespedes and J. Sun, "Mitigation of inverter-grid harmonic resonance by narrow-band damping," *IEEE J. Emerg. Sel. Topics Power Electron.*, vol. 2, no. 4, pp. 1024–1031, Dec. 2014.

[23] D. Yang, X. Ruan, and H. Wu, "Impedance shaping of the grid-connected inverter with LCL filter to improve its adaptability to the weak grid condition," *IEEEE Trans. Power Electron.* vol. 29, no. 11, pp. 5795–5805, Nov. 2014.

[24] S. Y. Park, C. L. Chen, J. S. Lai, and S. R. Moon, "Admittance compensation in current loop control for a grid-tie LCL fuel cell inverter," *IEEEE Trans. Power Electron.* vol. 23, no. 4, pp. 1716–1723, Jul. 2008.

[25] X. Wang, F. Blaabjerg, and P. C. Loh, "Virtual RC damping of LCL-filtered voltage source converters with extended selective harmonic compensation," *IEEE Trans. Power Electron.*, vol. 30, no. 9, pp. 4726–4737, Sep. 2015.

[26] J. Dannehl, F. W. Fuchs, S. Hansen, and P. B. Thogersen, "Investigation of active damping approaches for PI-based current control of grid-connected pulse width modulation converters with LCL filters," *IEEE Trans. Ind. Appl.*, vol. 46, no. 4, pp. 1509–1517, Jul./Aug. 2010.

[27] O. Brune, "Synthesis of a finite two-terminal network whose driving-point impedance is a prescribed function of frequency," *J. Math. Phy.* vol. 10, pp. 191–236, 1931.

[28] L. Harnefors, L. Zhang, and M. Bongiorno, "Frequency-domain passivity-based current controller design," *IET Power Electron.*, vol. 1, no. 4, pp. 455–465, Dec. 2008.

[29] L. Harnefors, X. Wang, A. G. Yepes, and F. Blaabjerg, "Passivity-based stability assessment of grid-connected VSCs—An overview," *IEEE J. Emerg. Sel. Topics Power Electron.*, vol. 4, no. 1, pp. 116–125, Mar. 2016.

[30] L. Harnefors, A. G. Yepes, A. Vidal, and J. Doval-Gandoy, "Passivity-based controller design of grid-connected VSCs for prevention of electrical resonance instability," *IEEE Trans. Ind. Electron.*, vol. 62, no. 2, pp. 702–710, Feb. 2015.

[31] X. Wang, F. Blaabjerg, and P. C. Loh, "Proportional derivative based stabilizing control of paralleled grid converters with cables in renewable power plants," in *Proc. IEEEEnergy Convers. Congr. Expo.*, 2014, 4917–4924.

[32] T. Messo, J. Jokipii, A. Makinen, and T. Suntio, "Modeling the grid synchronization induced negative-resistaor-like behavior in the output impedance of a three-phase photovoltaic inverter," in *Proc. 4th IEEE Int. Symp. Power Electron. Distrib. Gener. Syst.*, 2013, pp. 1–8.

[33] B. Wen, D. Boroyevich, R. Burgos, P. Mattavalli, and Z. Shen, "Analysis of D-Q small-signal impedance of grid-tied inverters," *IEEE Trans. Power Electron.* vol. 31, no. 1, pp. 675–687, Jan. 2016.

[34] R. Beres, X. Wang, F. Blaabjerg, C. L. Bak, and M. Liserre, "Comparative evaluation of passive damping topologies for parallel grid-connected converters with LCL filters," in *Proc. IEEE Int. Power Electron. Conf. (IPEC-Hiroshima 2014 - ECCE ASIA)*, 2014, pp. 3320–3327.

[35] J. C. Willems, "Dissipative dynamic systems, part I: General theory," *Arch. Ration. Mech. Anal.* vol. 45, pp. 321–351, 1972.

[36] A. Riccobono and E. Santi, "Comprehensive review of stability criteria for dc power distribution systems," *IEEE Trans. Ind. Appl.* vol. 50, no. 5, pp. 3525–3535, Spe./Oct. 2014.

[37] M. Huang, X. Wang, P. C. Loh, and F. Blaabjerg, "LLCL-filtered grid converter with improved stability and robustness," *IEEE Trans. Power Electron.* vol. 31, no. 5, pp. 3958–3967, May 2016.

[38] D. G. Holmes, T. A. Lipo, B. P. McGrath, and W. Y. Kong, "Optimized design of stationary frame three phase AC current regulators," *IEEE Trans. Power Electron.*, vol. 24, no. 11, pp. 2417–2426, Nov. 2009.

[39] R. D. Middlebrook, "Input filter design considerations in design and applications of switching regulators," in *Proc. IEEE Ind. Appl. Soc. Annu. Meeting*, 1976, pp. 366–382.

[40] R. Turner, S. Walton, and R. Duke, "A case study on the application of the Nyquist stability criterion as applied to interconnected loads and sources on grids," *IEEE Trans. Ind. Electron.* vol. 60, no. 7, pp. 2740–2749, Jul. 2013.
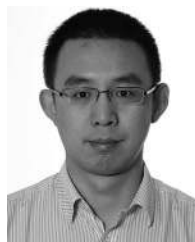
Xiongfei Wang (S'10–M'13) received the B.S. degree from Yanshan University, Qinhuangdao, China, in 2006, the M.S. degree from Harbin Institute of Technology, Harbin, China, in 2008, both in electrical engineering, and the Ph.D. degree in energy technology from Aalborg University, Aalborg, Denmark, in 2013.

Since 2009, he has been with the Aalborg University, Aalborg, Denmark, where he is currently an Associate Professor in the Department of Energy Technology. His research interests include modeling and control of grid-connected converters, harmonics analysis and control, passive and active filters, and stability of power electronic based power systems.

He received the IEEE Power Electronics Transactions Prize Paper award in 2014. He is the Associate Editor for the IEEE TRANSACTIONS ON INDUSTRY APPLICATIONS and the IEEE JOURNAL OF EMERGING AND SELECTED TOPICS IN POWER ELECTRONICS.

Frede Blaabjerg (S'86–M'88–SM'97–F'03) received the Ph.D. degree in electrical engineering from Aalborg University, Aalborg, Denmark, in 1992.

He was with ABB-Scandia, Randers, Denmark, from 1987 to 1988. He became an Assistant Professor in 1992, Associate Professor in 1996, and Full Professor of power electronics and drives in 1998. His current research interests include power electronics and its applications such as in wind turbines, PV systems, reliability, harmonics, and adjustable speed drives.

He has received the 17 IEEE Prize Paper Awards, the IEEE PELS Distinguished Service Award in 2009, the EPE-PEMC Council Award in 2010, the IEEE William E. Newell Power Electronics Award 2014, and the Villum Kann Rasmussen Research Award 2014. He was an Editor-in-Chief of the IEEE TRANSACTIONS ON POWER ELECTRONICS from 2006 to 2012. He is nominated in 2014 and 2015 by Thomson Reuters to be between the most 250 cited researchers in Engineering in the world.

Poh Chiang Loh received the B.Eng (Hons) and M.Eng degrees from the National University of Singapore, Singapore, in 1998 and 2000 respectively, and the Ph.D degree from Monash University, Melbourne, Vic, Australia, in 2002, all in electrical engineering.

His research interests include power converters and their grid applications.